Study of surfactant induced deformations at the interface of emulsion droplets by digital image analysis of droplet projections

Helena vom Stein, Dirk Volkmer

Study of Surfactant-Induced Deformations at the Interface of Emulsion Droplets by Digital Image Analysis of Droplet Projections

Helena vom Stein and Dirk Volkmer*

Emulsion droplets do not always have smooth surfaces. Under certain conditions, the formation of surface-active species at oil–water interfaces leads to interfacial instabilities that cause a spontaneous increase in the droplet surface area, which results in fascinating droplet morphologies. The specific system presented in this study consists of stearic acid encapsulated in an oil droplet and the quaternary ammonium surfactant cetyltrimethylammonium bromide in the aqueous phase. This system is studied by examining the deformation of single emulsion droplets hanging on a capillary tip. By using digital image analysis, the relative perimeters and fractal dimensions from the droplet outlines are calculated and the influences of several process parameters on their temporal development are studied. It is demonstrated that the surfactant concentration, pH value, salt addition, alcohol addition, and viscosity have a considerable impact on the droplet morphology and possible causes for this behavior are discussed. Through this study, important insights are gained into the deformation mechanism and kinetics that can potentially guide the future preparation of particles with special surface morphologies.

1. Introduction

The study of dynamic processes at liquid–liquid interfaces has long been a topic of special interest in emulsion science and technology. In recent years, surfactant-induced interfacial instabilities that cause deformations at oil–water interfaces have been the focus of several publications related to fundamental theoretical considerations[1] as well as investigations engaged in characterizing measurements.[2] Moreover, application-oriented research has been conducted with the goal of using interfacial deformations for the creation of novel

H. vom Stein, D. Volkmer
Solid State and Materials Chemistry
University of Augsburg
Universitaetsstrasse 1, D-86159 Augsburg, Germany
E-mail: dirk.volkmer@physik.uni-augsburg.de

The ORCID identification number(s) for the author(s) of this article can be found under https://doi.org/10.1002/admi.202200264.

particulate materials with exceptional properties.[3]

The instabilities that develop at the oil–water interface result from a massive decrease in the interfacial tension to values close to zero or even transiently negative.[1c,4] The adsorption of surfactants typically reduces the surface tension until the interface is fully occupied without causing an expansion of the interface. However, chemical reactions between non-miscible liquids that generate surface-active species directly at the interface can cause an overpopulation that makes the effective surface tension negative.[1b] In this case, it is energetically favorable to increase the droplet surface area, which frequently causes the detachment of numerous smaller droplets and is commonly referred to as "spontaneous emulsification."[5] However, if the interface itself possesses elastic properties, a multitude of shapes and morphologies may evolve. In some cases, the droplets adopt complex regular shapes, such as icosahedra, octahedra, or hexagonal platelets, which sometimes even develop long tails at their edges.[3e,6] In other cases, the droplets can develop random bumps that grow into spines and eventually break off the surface as smaller droplets or elongated aggregates.[3b,c,g,k] Through careful choice of chemical components and process parameters, these deformed droplets can be solidified to form particles of various shapes and surface morphologies.[3a,b,g] Such particles are of high interest for both fundamental and applied research because their morphology significantly affects the physical properties of the particles.[7] For example, the surface roughness plays a substantial role in particle–cell interactions in drug delivery[8] or tissue engineering,[9] and the porosity and specific surface area are crucial in applications, such as catalysis[10] and separation.[11]

The system described in this study is an example of an interfacial instability that features droplets with a spinose surface. It consists of a fatty acid in an oil droplet and cetyltrimethylammonium bromide (CTAB) in the surrounding aqueous phase. The reaction that causes interfacial overpopulation is the deprotonation of arachidic acid molecules that are in contact with water. Additionally, surface-active CTA^+ cations from the aqueous phase penetrate the interface and promote interfacial overpopulation. Simultaneously, the dissimilar surface-active species form an elastic layer at the interface, leading to the formation of spines instead of the simple detachment of smaller droplets. In previous

studies, we have shown that this system can be used to produce solid particles with several different morphologies.[3a,b] The strategy for shaping particle surfaces through interfacial instability involves freezing the deformation in a non-equilibrium state through polymerization reactions in the bulk of the droplet. For precise control of the particle morphology, it is necessary to have a good understanding of the process dynamics and the qualitative and quantitative influence of the experimental parameters. Conventional methods that study interfacial phenomena include drop profile analysis tensiometry or the Langmuir–Blodgett technique. The latter has been used previously to study the penetration kinetics of CTAB from an aqueous subphase into fatty acid monolayers at the air–water interface.[12] However, these methods only study the interfacial tension and not the microscopic deformations at the liquid–liquid interfaces.

In this study, we investigated the deformation of single droplets hanging on a capillary tip using a horizontal microscope and digital image analysis. We derived quantitative shape factors from droplet projections and studied the influences of several process parameters on their temporal development. Through these investigations, we gain important insights into the deformation mechanism and kinetics that can potentially guide the future preparation of particles with certain surface morphologies.

2. Experimental Section

2.1. Materials and Preparation

Injections were performed at ambient conditions using two different amphiphilic species in the oil and aqueous phases. Several amphiphilic species were used for this purpose, which

are listed in **Table 1**. All the chemicals were used as received without further purification.

2.1.1. Preparation of Oily Phases

The nonpolar phases were prepared by gentle heating of the solvent to ≈50 °C to facilitate the dissolution process. The solutions then cooled down to ambient conditions and were left for equilibration for at least 24 h. Within that time and after no crystallization has been observed for any of the tested solutions. The standard nonpolar phase was prepared using bromocyclohexane (BCH, Merck, 98%, mp = −56.5 °C[13]) as the solvent and stearic acid (SA) as the surfactant at a concentration of 20 mmol L^{-1}. For the concentration studies, SA solutions were prepared at concentrations of 5, 10, 20, and 40 mmol L^{-1}. All the nonpolar phases containing the other amphiphilic species listed in Table 1 were also prepared using BCH at a concentration of 20 mmol L^{-1}. For the test series with variation of the solvent, SA (20 mmol L^{-1}) was dissolved in chlorobenzene (Fluka), benzene (Merck), chlorocyclohexane (Merck), cyclohexane (Merck), tetrahydronaphthalene (Merck), chloroform (Alfa Aesar), and toluene (Aldrich).

2.1.2. Preparation of Aqueous Phases

Ultrapure water with a resistance of at least 18.2 MΩ cm was used for the preparation of all the aqueous solutions. The standard aqueous phase was prepared using CTAB as the surfactant at a concentration of 50 µmol L^{-1}. For the concentration studies, aqueous solutions of CTAB at concentrations of 6.25, 12.5, 25, 50, 100, 200, 500, and 2000 µmol L^{-1} were prepared.

Table 1. Amphiphilic species used in this study.

Chemical (abbreviation)	Formula	CAS	Supplier	Purity	mp[a] [°C]
Dissolved in aqueous phase					
Cetylyltrimethylammonium bromide (CTAB)	$CH_3(CH_2)_{15}N(CH_3)_3Br$	57-09-0	Merck	≥99%	230
Didodecyldimethylammonium bromide (DDDAB)	$[CH_3(CH_2)_{11}]_2N(CH_3)_2Br$	3282-73-3	Aldrich	98%	157–162
Dimethyldioctadecylammonium bromide (DODAB)	$[CH_3(CH_2)_{17}]_2N(CH_3)_2Br$	3700-67-2	Fluka	≥98%	≈160
Dodecyltrimethylammonium bromide (DTAB)	$CH_3(CH_2)_{11}N(CH_3)_3Br$	1119-94-4	Aldrich	99.0%	246 (dec.)
Ethylhexadecyldimethylammonium bromide (ECDAB)	$C_2H_5N(CH_3)_2C_{16}H_{33}Br$	124-03-8	Merck	Synthesis	178–186
Sodium dodecyl sulfate (SDS)	$CH_3(CH_2)_{11}OSO_3Na$	151-21-3	ITW	>99%	204–207
Stearyltrimethylammonium bromide (STAB)	$CH_3(CH_2)_{17}N(CH_3)_3Br$	1120-02-1	Merck	98%	≈250 (dec.)
Tetramethyltrimethylammonium bromide (TTAB)	$CH_3(CH_2)_{13}N(CH_3)_3Br$	1119-97-7	VWR	>98%	245–250
Dissolved in nonpolar phase					
Arachidic acid (AA)	$CH_3(CH_2)_{18}COOH$	506-30-9	Aldrich	>99.0%	74–76
Lauric acid (LA)	$CH_3(CH_2)_{10}COOH$	143-07-7	Aldrich	Synthesis	43–45
Myristic acid (MA)	$CH_3(CH_2)_{12}COOH$	544-63-8	Aldrich	≥99%	52–54
Octadecylamine (ODA)	$CH_3(CH_2)_{17}NH_2$	124-30-1	Merck	Synthesis	50-52
Palmitic acid (PA)	$CH_3(CH_2)_{14}COOH$	57-10-3	Merck	≥99%	61–62.5
Stearic acid (SA)	$CH_3(CH_2)_{16}COOH$	57-11-4	BDH	>97%	69.3[13]

[a]Melting point as indicated by supplier if no reference is given.

**ADVANCED
SCIENCE NEWS**

www.advancedsciencenews.com

**ADVANCED
MATERIALS
INTERFACES**

www.advmatinterfaces.de

Aqueous solutions of the other surfactants listed in Table 1 had a concentration of 50 μmol L^{-1}.

2.1.3. Parameter Studies

Several test series were performed to investigate the influence of pH, ionic strength, ethanol addition, and viscosity. The aqueous CTAB solution (50 μmol L^{-1}) had a pH between 6 and 7 because the ultrapure water used for its preparation was slightly acidic. The pH value was adjusted to 2 and 5 by adding 10 mmol L^{-1} or 100 μmol L^{-1} hydrochloric acid (HCl) and to 12 or 7 by adding the same concentrations of sodium hydroxide (NaOH) to the as-prepared 50 μmol L^{-1} CTAB solution. For variation of the ionic strength, 1 or 10 μmol L^{-1} sodium chloride (NaCl) was dissolved in the as-prepared 50 μmol L^{-1} CTAB solution. Aqueous solutions of ethanol were prepared using 5 and 10 vol% ethanol. The shear viscosity of the oily phase was adjusted by dissolving 10, 20, 30, 40, or 50 wt% of polystyrene (PS) with a mass average molar mass of 35 000 g mol^{-1} (Aldrich) in BCH containing 20 mmol L^{-1} SA.

2.1.4. Viscosity Measurements

PS with a mass average molar mass of 35 000 g mol^{-1} (Aldrich) was dissolved to concentrations of 10, 20, 30, 40, or 50 wt% in BCH containing 20 mmol L^{-1} SA. Viscosity measurements were performed on an Anton Paar rheometer (MCR302) at a temperature of 20 °C using a plate–plate geometry (plate diameter: 25 mm, plate distance: 0.45 mm) in rotation with a controlled shear rate of 100 s^{-1}. All measurements were performed in triplicate.

2.2. Methods for Capturing Digital Images

2.2.1. Setup

A custom-made optical bench capable of functioning as a horizontal light microscope was used to observe the shape of each oil droplet surrounded by the aqueous phase (**Figure 1**). The droplet was injected into the aqueous phase using a zero dead volume syringe (0.5 μL, 7000.5 ASRN Hamilton) and was allowed to hang at the tip of the needle for observation. The syringe was oriented vertically and mounted on a linear positioning system that was adjustable in all the three spatial dimensions by micrometer screws (MT 50-6-XYZ, Owis). The injection was performed in a transparent disposable PS cuvette with a capacity of 2.5 – 4.5 mL (VWR) which was situated in a custom-made matte black sample holder to minimize reflection. Köhler illumination in the plane of the droplet was achieved using an illumination system equipped with a cold LED light source (KL 300 LED, Schott) including a focusing lens, luminous field diaphragm, and condenser lens with an aperture diaphragm. Ground glass and yellow filters were used to further optimize the illumination and resolution. The objective (5X Mitutoyo Plan Apo Infinity Corrected Long Working Distance Objective) had a numerical aperture of 0.14 and focal length of 40 mm. A maximum resolution of 2.6 μm was achieved with the described illumination and used objective. Additionally, the optical system of the bench comprised a 70XL lens system (Optem), which consisted of an objective dual focus module, an Upper Detented Zoom module, and a 1.0× TV tube. Photographs were captured using a complementary metal oxide semiconductor (CMOS) Camera (E3CMOS Series C-mount USB3.0 by ToupTek) comprising a 1/1.8″ sensor with a hardware resolution of 6.3M, which corresponded to physical pixel dimensions of 2.4 × 2.4 μm. At a magnification of 5×, one pixel corresponded to 0.42 μm. The recorded images have dimensions of 3072 × 2048 pixels or 1290.24 × 860.16 μm. The ToupView software was used for image acquisition with a predefined exposure time of 94 ms.

2.2.2. Injection Procedure

First, the transparent cuvette was filled with 3 mL of the aqueous phase. Gentle tapping of the filled cuvette on the table helped to remove the small gas bubbles on the cuvette walls. After positioning the cuvette in the sample holder, 0.06 μL of the respective oil phase was drawn using the syringe.
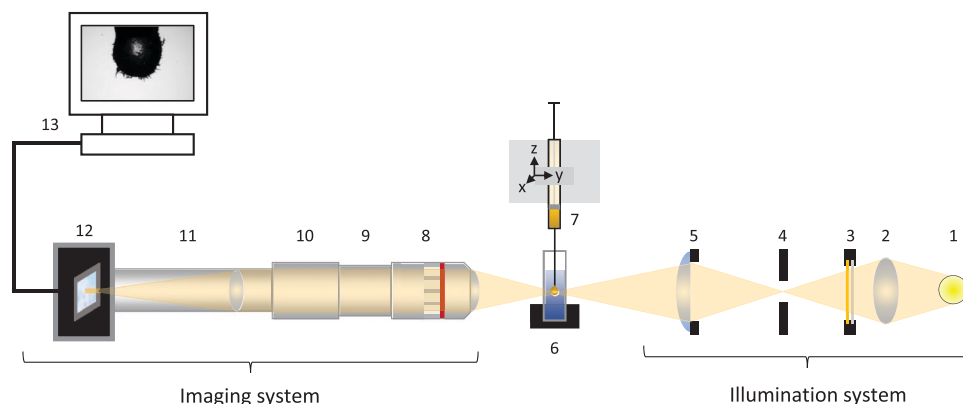

Figure 1. Schematic of the horizontal microscope setup used for injection experiments. 1) Light source, 2) Collector lens, 3) Filters, 4) Luminous field diaphragm, 5) Condenser lens with aperture diaphragm, 6) Cuvette with aqueous phase, 7) Positioning system with syringe containing oil phase, 8) 5× Objective, 9) Focus module, 10) Zoom module, 11) TV tube, 12) CMOS Camera, 13) PC with ToupView software.

2200264 (3 of 13)

ADVANCED
SCIENCE NEWS
www.advancedsciencenews.com

ADVANCED
MATERIALS
INTERFACES
www.advmatinterfaces.de

Subsequently, the steel needle was wiped with a lint-free tissue to prevent its wetting through contact with the oil phase, which would distort the droplet. The syringe was mounted at the lowest position of the syringe holder with the needle dipped in the aqueous phase. The position of the needle was adjusted by turning the micrometer screws of the positioning system such that the tip of the needle was at the top of the visible field and in focus. The time-lapse recording was started immediately before the injection of the entire syringe content, which would result in a droplet diameter of approximately 450 µm. Images were recorded every 5 s. Injections with the same parameter set were performed three times.

2.3. Image processing for shape quantification

Digital image processing and analysis of the shape parameters of each image comprising the time-lapse recordings were performed using the ImageJ program.[14] An ImageJ macro with the steps necessary for image processing and particle analysis was realized. The fractal dimension (FD) was calculated using the ImageJ plugin FracLac[15] in a separate step. A schematic illustration of the procedure for image analysis is shown in **Figure 2**. Pre-processing of the original grayscale images was achieved using the following steps.

I)   A background corrected image was acquired by dividing the original image by a background image that was captured using the same illumination through the water-filled cuvette without a droplet in the field of view.

II) The translucent center of the droplet projection was removed by artificially overexposing the droplet, creating a corresponding region of interest, and filling this region with black color in the background-corrected image. Artificial

overexposure was achieved by performing Gaussian blurring with radius 10, followed by multiplication of the image by the value 10 and performing an "auto threshold" adjustment using the default method.

III) The image was cropped to remove the capillary tip from the field of view. Segmentation of the image was performed using the "auto local threshold" function by applying the "Bernsen"[14] method with radius 20. The image mask obtained in this step was further used for the analysis of the perimeter and droplet count.

IV) An outline of the segmented image from the previous step (excluding small droplets) was created to analyze the FD.

The pre-processed images were further used to compute the following shape parameters:

A) Perimeter (*P*): The ImageJ particle analysis tool with a size exclusion of particles smaller than 50 000 µm^2 was used to obtain the perimeter of the mother droplet.

B) Droplet count (*C*): The number of ejected droplets was analyzed by performing another particle analysis on all the particles larger than 3 µm in diameter, excluding the particles on the edges of the image. This excluded the mother droplet.

C) Fractal dimension (*FD*): The outline of the segmented image was used to perform a fractal analysis using the FracLac box-counting method. Box counting was performed with box sizes ranging from 3 to 350 pixels with 6 grid positions for each box size.

The FD is a mathematical concept for assigning a dimensional value to objects with complex geometries. A straight line has a dimension of 1, and a plane-filling curve has a dimension of 2. However, a very fractal line whose length increases upon
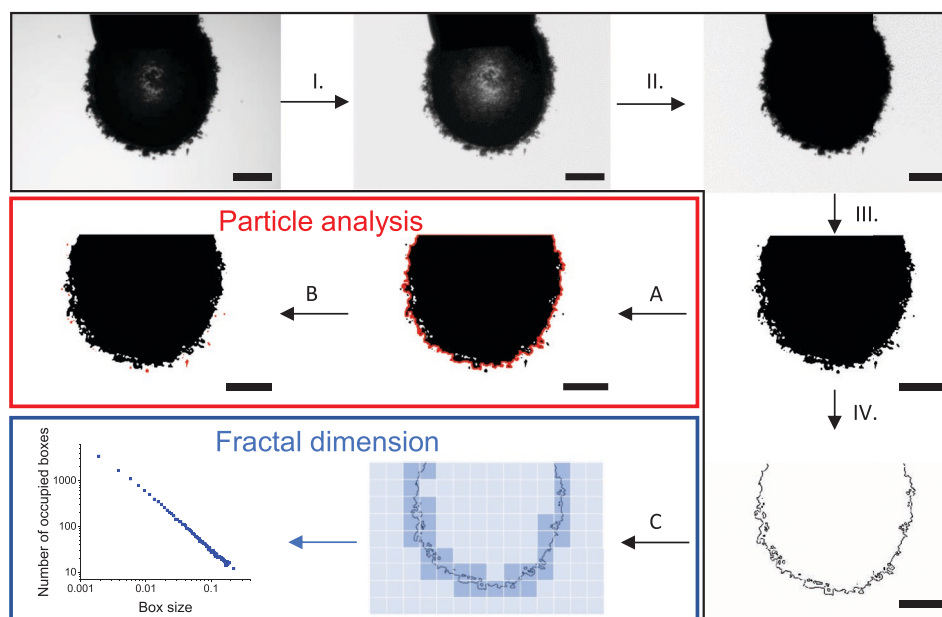

Figure 2. Schematic representation of the procedure used for digital image analysis. The numbering refers to the descriptions in the main text. The scale bar corresponds to 200 µm.

**ADVANCED
SCIENCE NEWS**

www.advancedsciencenews.com

**ADVANCED
MATERIALS
INTERFACES**

www.advmatinterfaces.de

zooming in, such as a coastline, has a dimension between 1 and 2.[16] The FD as a second parameter in addition to the perimeter to describe the outline of the droplet with the goal of differentiating between very spiky droplets and droplets with smoother surfaces, were used. One of the most popular methods for calculating the FD from an image is the box-counting method. In this method, a binary image was covered by a regular grid with box sizes of length r, and the number of boxes N that contain foreground pixels was counted. This procedure was repeated with boxes of different sizes to obtain the function $N(r)$. The FD is then given by the slope of the logarithmic regression line for N and r.[15,17]

$$FD = -\lim_{r \to 0} \frac{\log(N(r))}{\log(r)} \quad (1)$$

After all the images corresponding to one injection were analyzed as described above, the time-lapsed recordings were used to study the temporal development of the shape parameters. The obtained values for the perimeter, P were used to calculate the relative perimeter P_{rel} by dividing P by the starting perimeter, P_0. The growth rate G, was calculated as the average slope of the curve $P_{rel}(t)$ from the starting point, $P_{rel}(t_0) = 1$ to the maximum value, $P_{max}(t_{max})$:

$$G = \frac{P_{max} - 1}{t_{max}} \times 100\% \quad (2)$$

and was given in % min^{-1}.

2.4. Statistical Analysis

Injection experiments with the same parameter set have been performed in triplicate (except for 500 and 2000 μmol L^{-1} CTAB solutions, which have been performed once). The curves that were obtained for each of the shape parameters $P_{rel}(t)$, FD(t), and $C(t)$ for the injections with the same parameter set were averaged to create the curves $\overline{P}(t)$, $\overline{FD}(t)$ and $\overline{C}(t)$, which are depicted in the results part. The calculation of the averaged curves was performed using the software "OriginPro" and the "Average multiple curves" function, by employing a linear interpolation between the data points. The standard deviation of the averaged curves is shown as colored shades in the diagrams.

The arithmetic means of the extreme values for the shape parameters of each parameter set were determined by identifying the extreme values for the individual injections from $P_{rel}(t)$ and FD(t) and calculating their arithmetic mean as $\overline{P}_{max}$, $\overline{t}_{max,P}$ $\overline{FD}_{max}$ and $\overline{t}_{max,FD}$ and $\overline{G}$.

The arithmetic mean for the viscosity has been calculated from three separate measurements.

The standard deviation was calculated using the following equation.

$$s = \sqrt{\frac{1}{n-1} \sum_{i=1}^{n} (x_i - \overline{x})^2} \quad (3)$$

3. Results and Discussion

3.1. Proof of Concept

The spine-forming instability at the interface of a droplet of BCH containing SA in an aqueous solution of CTAB was observed in injection experiments on an optical bench and analyzed via digital image analysis. As a proof of concept, this section describes the temporal development of the quantitative shape parameters, P, FD, and C obtained from the time-lapse recordings. **Figure 3** depicts the shape development of a droplet containing 20 mmol L^{-1} SA in an aqueous solution of 50 μmol L^{-1} CTAB over the course of 70 min using three different parameters. Video S1, Supporting Information, shows the time-lapse recording of the projected droplet. According to the results, the values of $\overline{P}$ and $\overline{FD}$ reached a maximum at 6.4 min after the start of the injection. At this point, the longest spines developed on the droplet surface. Thereafter, the spines started to collapse and $\overline{P}$ and $\overline{FD}$ decreased. The very distinct peak in the development of these shape parameters is therefore a reliable measure for the comparison of injections with different parameters. The droplet count does not show a peak because the number of ejected droplets increases continuously when the spines detach from the interface.

3.2. Influence of the Surfactant Concentration

The influence of the concentrations of SA and CTAB on the development of the droplet shape was tested in repeated injections. All the injections that were performed with CTAB concentrations up to 100 μmol L^{-1} had a similar course and exhibited a peak in the temporal perimeter development. **Figure 4** illustrates the maximum relative perimeter $\overline{P}_{max}$ and the growth rate $\overline{G}$ corresponding to different combinations of surfactant concentrations. Each value represents the mean of at least three injections. Table S2, Supporting Information, lists all the numerical values for $\overline{P}_{max}$, $\overline{t}_{max,P}$ $\overline{FD}_{max}$ and $\overline{t}_{max,FD}$ and $\overline{G}$. The highest values of the relative perimeter were observed for SA concentrations above 5 mmol L^{-1} and CTAB concentrations of 50 and 100 μmol L^{-1}, where the developed spines cause at least a duplication of the droplet perimeter. High values of the relative perimeter were also measured at CTAB concentrations of 6.25 μmol L^{-1}. However, these values occur much later during the droplet injection, which results in a lower growth rate than for high CTAB concentrations. The maximum fractal dimension $\overline{FD}_{max}$, which is shown in Figure S2, Supporting Information, behaves similar to the maximum relative perimeter. Both the surfactant concentrations have an influence on the growth rate, which is highest for a SA concentration of 40 mmol L^{-1} and a CTAB concentration of 50 μmol L^{-1}. With higher concentrations of SA in the oil phase and CTAB in the aqueous phase, the interface is filled more rapidly with amphiphilic molecules. On the one hand, more surface-active molecules are readily available to be included in the interface, and on the other hand, the dissociation of the SA molecules in contact with water leads to an electrostatic attraction between them and the cationic CTAB molecules. The latter increases the rate at which the CTAB molecules are included in the interfacial membrane.[12]
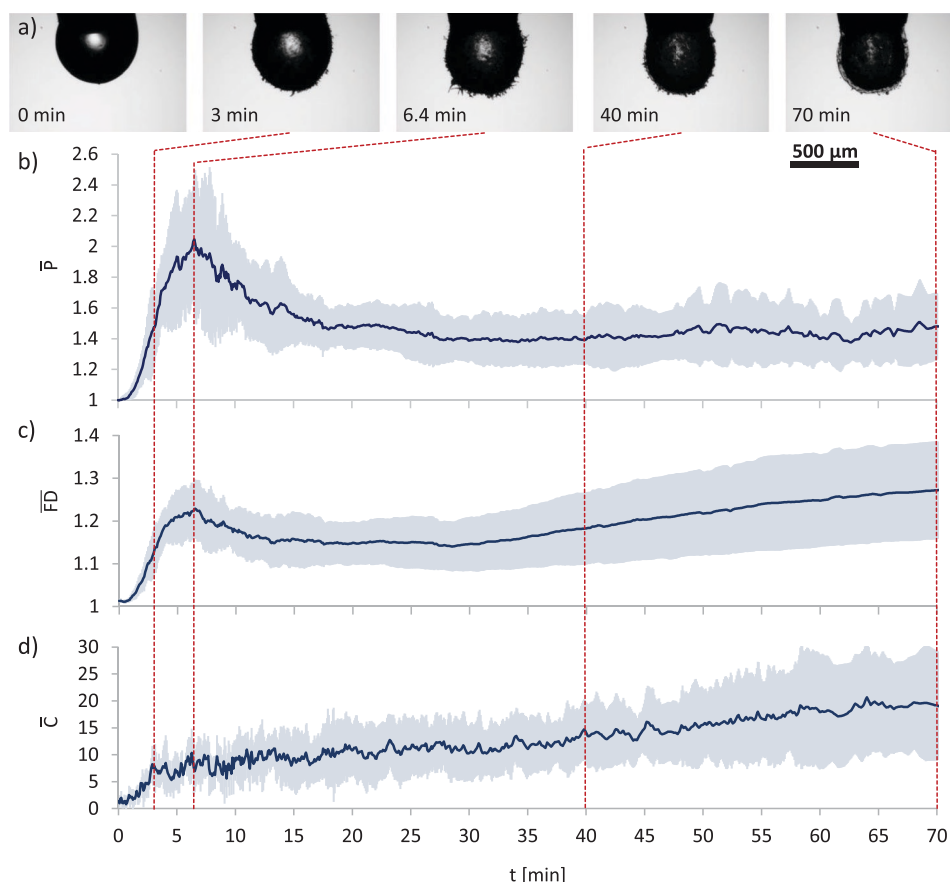
**ADVANCED
SCIENCE NEWS**

www.advancedsciencenews.com

**ADVANCED
MATERIALS
INTERFACES**

www.advmatinterfaces.de

Figure 3. Shape development of a droplet containing 20 mmol L⁻¹ SA in an aqueous solution of 50 µmol L⁻¹ CTAB over the course of 70 min. a) The micrographs show the droplet corresponding to one representative injection at different points in time. Each graph for the temporal development of b) the perimeter, c) the fractal dimension and d) the droplet count represents the mean of five separate injections with the shaded area representing the standard deviation.

The droplet morphology at $\overline{t}_{\text{max,P}}$ for different combinations of surfactant concentrations is depicted in **Figure 5**. For SA concentrations above 5 mmol L⁻¹ the morphology depends only marginally on the SA concentration, but strongly on the CTAB concentration. CTAB concentrations of 6.25 µmol L⁻¹ result in thick and occasionally very long spines, whereas CTAB concentrations of 50 and 100 µmol L⁻¹ produce thinner, more uniform and evenly distributed spines. At medium

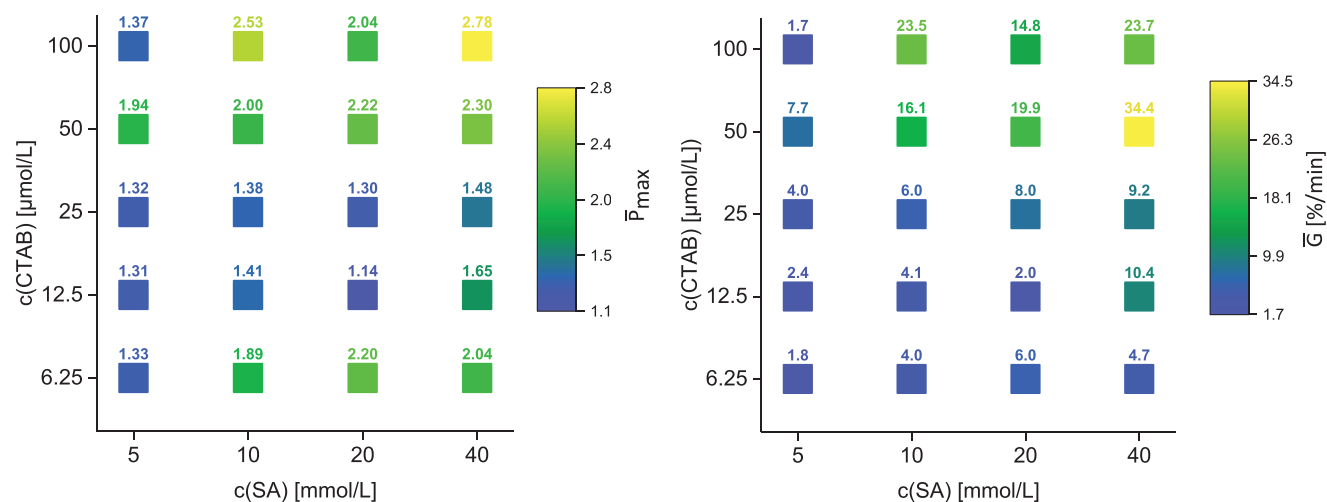**Figure 4.** Maximum relative perimeters $\overline{P}_{\text{max}}$ (left) and growth rates $\overline{G}$ (right) corresponding to different combinations of surfactant concentrations $c(SA)$ and $c(CTAB)$ on a logarithmic scale.

**ADVANCED
SCIENCE NEWS**

www.advancedsciencenews.com

**ADVANCED
MATERIALS
INTERFACES**

www.advmatinterfaces.de

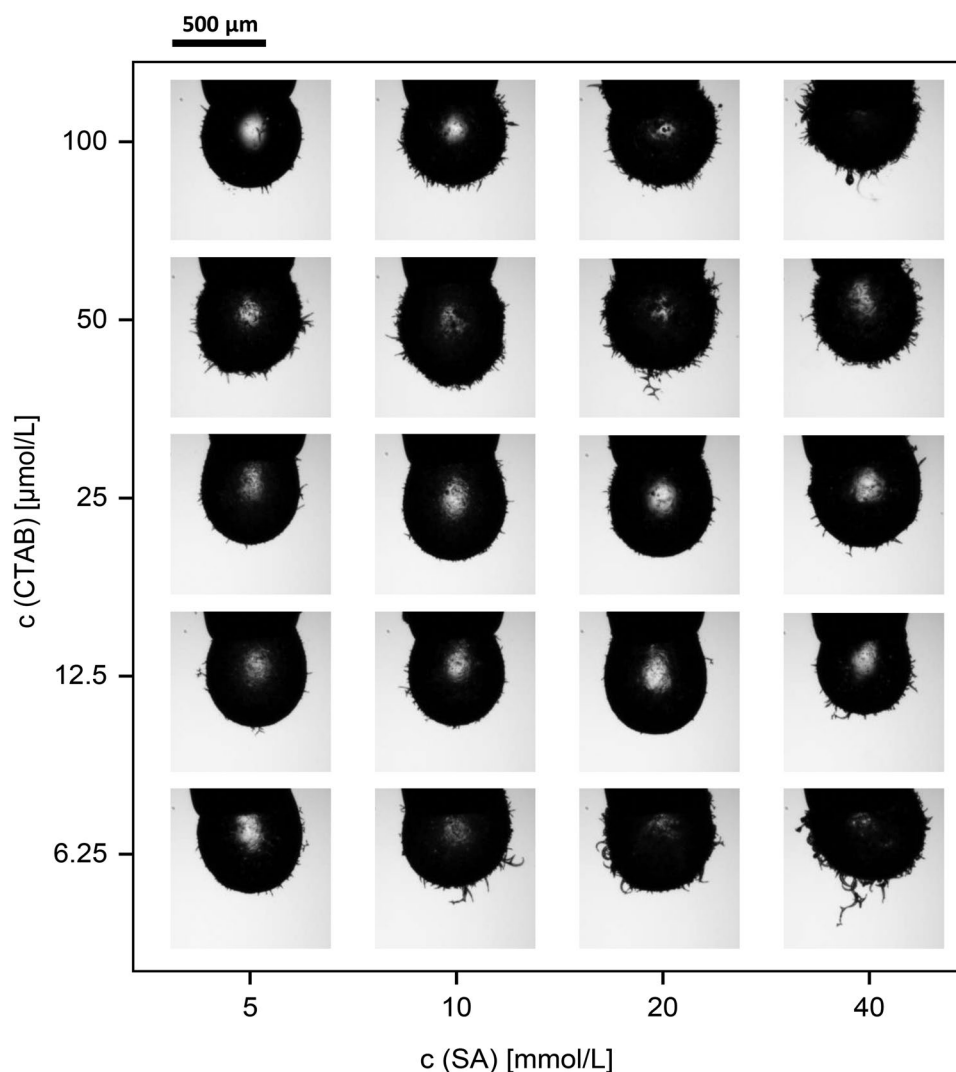**Figure 5.** Droplet morphology at $\bar{t}_{max,P}$ for different combinations of surfactant concentrations c(SA) and c(CTAB).

CTAB concentrations the droplet surface is only sparsely covered with short spines.

At CTAB concentrations exceeding 100 µmol L^{-1}, the development of the droplet morphology over time changes notably, and the shape curves have a different course than that shown in Figure 3. Figure 4 shows that CTAB concentrations of 50 and 100 µmol L^{-1} result in high values for the maximum perimeter. However, **Figure 6** shows that if the CTAB concentration is increased further, the maximum perimeter first decreases until 200 µmol L^{-1} and then increases again. This behavior was confirmed by the FD shown in Figure S4, Supporting Information. The droplet counts, which are also shown in Figure 6, for 500 and 2000 µmol L^{-1}, are two orders of magnitude higher than those for lower CTAB concentrations. This is attributed to the development of different morphologies. The degree of spine formation was found to decrease up to 200 µmol L^{-1} CTAB. Up to 500 µmol L^{-1} CTAB, the droplet became progressively less translucent in the center, which indicates increased surface roughness. At 500 µmol L^{-1} CTAB, the droplet expands strongly, which accounts for the different

course of the droplet perimeter curve without a distinct peak. At a concentration of 2000 µmol L^{-1}, the droplet becomes translucent again and is quickly surrounded by a corona of a contiguous aggregate, which by the digital image analysis process is recognized as a perimeter increase at the beginning, and as a strongly increasing droplet count in the course of the injection. Video S5, Supporting Information, shows the aggregate formation of a droplet containing 20 mmol L^{-1} SA in an aqueous solution of 2000 µmol L^{-1} CTAB.

The influence of the surfactant concentration on the growth rate and droplet morphology suggests that the adsorption at the interface plays a crucial role in the deformation mechanism.

At this point, it is worth noting, that although the melting point of SA lies above the measurement temperature no crystallization of SA takes place in the bulk of the nonpolar phase because the solution is unsaturated. The same is true for the aqueous CTAB solution. However, the adsorption of amphiphilic molecules at an interface often leads to the condensation of a 2D monolayer, which typically exhibits a viscoelastic behavior.[18] When SA and CTAB molecules populate
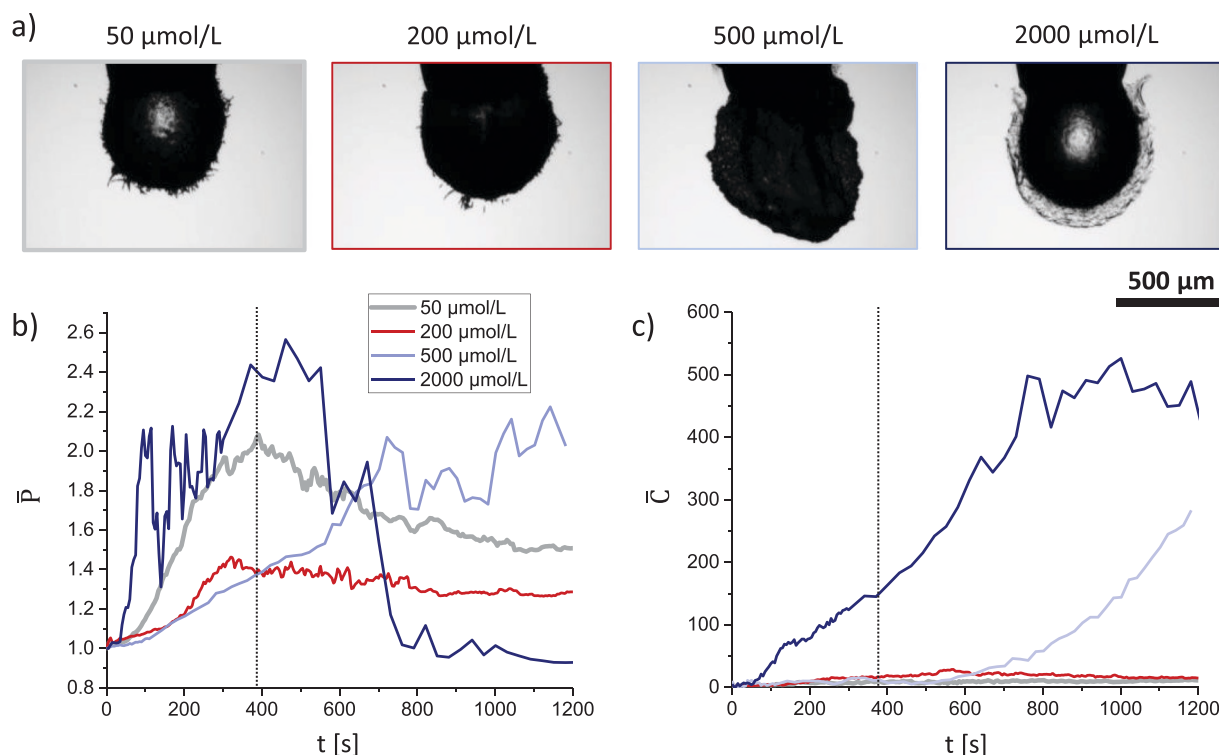
**ADVANCED
SCIENCE NEWS**

www.advancedsciencenews.com

**ADVANCED
MATERIALS
INTERFACES**

www.advmatinterfaces.de

Figure 6. Injections with 20 mmol L^{-1} SA and high CTAB concentrations. a) Micrographs of droplets after 380 s, b) perimeter development, and c) number of detected droplets. The standard deviation is not shown in the diagrams for simplicity.

the surface of the droplet, they form an elastic interfacial membrane, which inhibits the detachment of small droplets when the interfacial area starts to increase and instead leads to the formation of spines. The composition of the interfacial membrane depends on the concentrations and adsorption dynamics of the dissimilar surfactants and influences the viscoelastic properties of the membranes.[18b,19] We hypothesize that the viscoelasticity of the interfacial membrane is a critical parameter responsible for the development of different droplet morphologies.

In the following sections, the influence of several other parameters on the shape development of droplets created using 50 µmol L^{-1} CTAB and 20 mmol L^{-1} SA as the injection content is explored.

3.3. Influence of the pH Value

SA has low solubility in water[20] and has a low tendency to leave the oil droplet or interface. Its dissociation strongly depends on the pH of the surrounding aqueous solution.[12,21] Additionally, the dissociation reaction of SA is essential for the development of the interfacial instability. In an acidic aqueous phase (pH 2), the SA molecules present at the droplet surface do not deprotonate, thereby preventing the chemical reaction that produces the surface-active species directly at the interface. As a consequence, no overpopulation occurs at the interface, and the interfacial instability is not initiated regardless of whether CTAB molecules are present in the aqueous phase

(Figure S6, Supporting Information). In contrast, in basic aqueous solutions (pH 12), the SA molecules at the interface completely dissociate, and the interface is overpopulated with surface-active molecules. In this case, even in the absence of CTAB, the droplet disassembles into a myriad of tiny droplets (Figure S6, Supporting Information). This phenomenon has been reported for various fatty acids in different studies and is referred to as "spontaneous emulsification".[5] The dissociation of the fatty acid and the resulting overpopulation at the interface can be regarded as the driving force for the expansion of the interfacial area by droplet ejection. When CTAB is present in the highly alkaline aqueous phase surrounding the droplet, it has no influence on the disassembly of the droplet. In that case, the spontaneous emulsification occurs before a sufficient adsorption of CTAB molecules on the interface can take place and thereby modifying its viscoelastic properties. As stated above, we suggest that the presence of an elastic monolayer at the interface is necessary for the occurrence of spines between the initiation of the deformation and the detachment of the droplets. Another behavior emerges when only slightly alkaline or acidic conditions are employed. The estimated pK_a of SA is 4.7 ± 0.5[22] which implies that even in a 50 µmol L^{-1} CTAB solution, which has a pH of 6, the majority of the SA molecules will dissociate. **Figure 7** illustrates that in an injection system composed of 50 µmol L^{-1} CTAB and 20 mmol L^{-1} SA, a change in pH drastically influenced the shape development of the droplet. At a pH of 7, small oil-filled droplets formed at the droplet surface and detached quickly from the interface, which resulted in a drastic increase in the
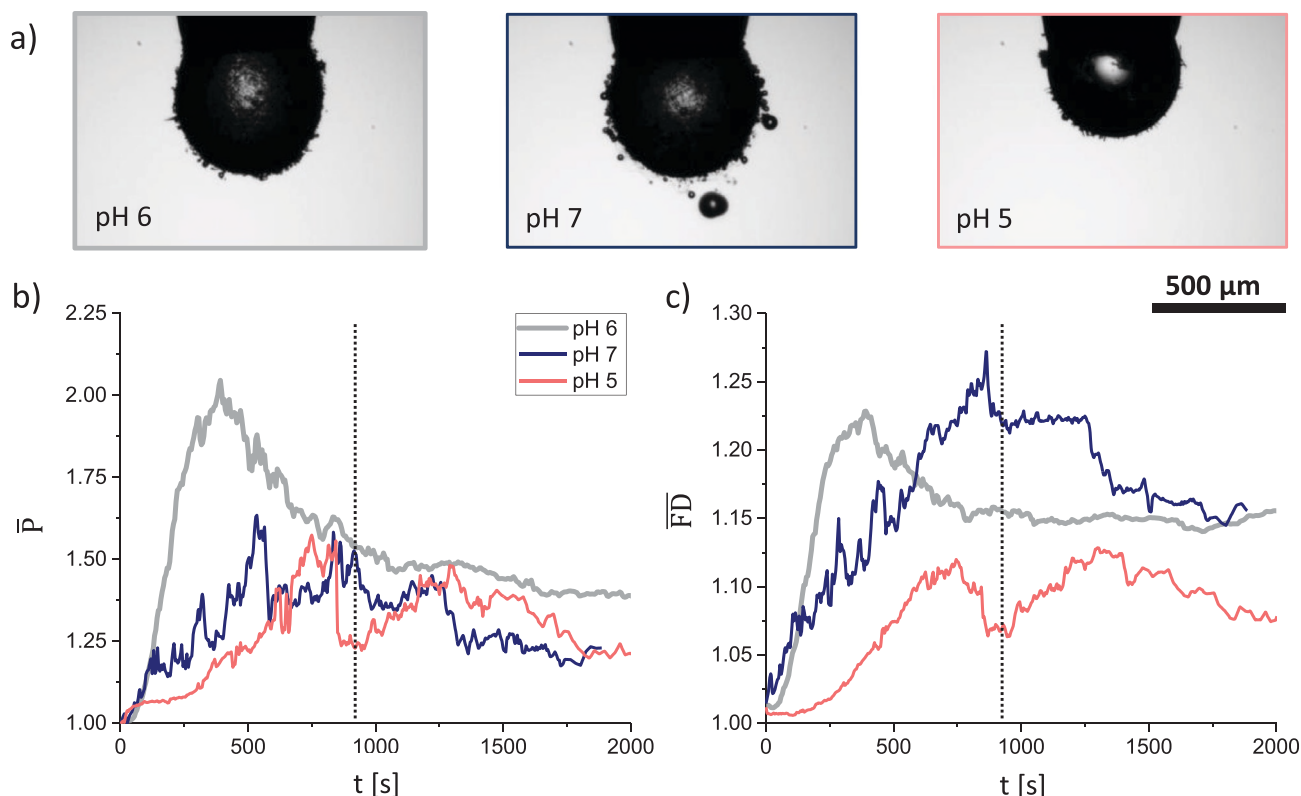
ADVANCED
SCIENCE NEWS

www.advancedsciencenews.com

ADVANCED
MATERIALS
INTERFACES

www.advmatinterfaces.de

Figure 7. Influence of the pH value on an injection system comprising 50 µmol L^{-1} CTAB and 20 mmol L^{-1} SA. a) Micrographs of representative droplets after 900 s, where the morphology difference is evident to the naked eye. Development of b) the relative perimeter, and c) the fractal dimension. The standard deviation is shown in the corresponding diagrams in Figure S7, Supporting Information.

droplet count (Figure S7, Supporting Information). In this case, the shape of the surface deformation resembles that of spheres rather than spines. This explains the observation that, at 900 s, the perimeter is similar to and the FD is considerably higher than that of the droplets at pH 6. An instability was also observed at a pH of 5; however, it occurred at a lower rate and only a few spines were observed, which manifested in lower values for the FD and perimeter.

3.4. Influence of the Ionic Strength

Figure 8 depicts the perimeter development of the projected droplet when NaCl was added to the 50 µmol L^{-1} aqueous solution of CTAB. This illustrates that even small additions of salt are sufficient to alter the process notably. Salt addition resulted in a smaller maximum perimeter. The effect of salt on the droplet morphology is similar to that observed for CTAB concentrations above 100 µmol L^{-1}. With increasing salt content, the morphology of the droplets becomes less spiky and less translucent in the center, which signifies a rough surface on a smaller scale. Generally, in aqueous solutions of ionic surfactants, the addition of salt increases the adsorption of surfactant molecules on hydrophobic surfaces.[21,23] This behavior is attributed to the entropy loss on adsorption caused by the presence of salt, which facilitates the migration of ionic amphiphilic molecules and their counter ions to the interface without

creating salt-depleted regions in the solution. Hence, the salt concentration affects the composition and the viscoelastic properties of the interfacial membrane, similarly to the CTAB concentration.

3.5. Influence of Ethanol Addition

Figure 9 illustrates the influence of the addition of a short chain alcohol (ethanol) in the aqueous phase on the shape development of the droplet comprising 20 mmol L^{-1} SA and 50 µmol L^{-1} CTAB. Increasing amounts of ethanol between 0 and 10 vol% reduced the formation of long spines, hence the maximum perimeter. Ethanol concentrations above 10 vol% inhibited the formation of stable droplets. Ethanol acts as a co-solvent and increases the solubility of BCH in water,[24] which has an influence on the formation of a stable oil/water-interface, thereby hindering the development of the spine-forming instability.

3.6. Influence of the Viscosity

Another important parameter that influences the degree of spine formation is the shear viscosity of the nonpolar phase. The shear viscosity was adjusted by dissolving different amounts of PS in BCH containing 20 mmol L^{-1} of SA. PS
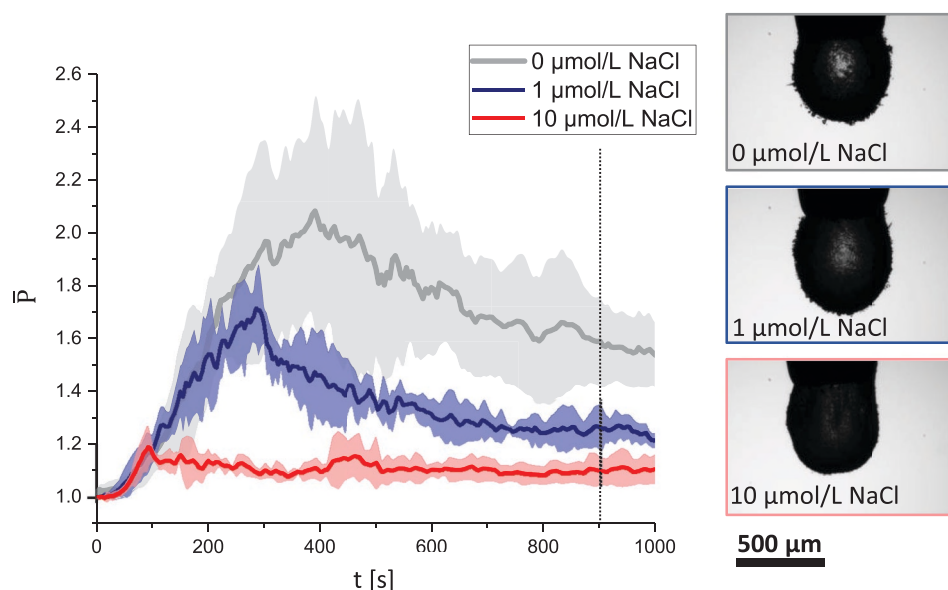
**ADVANCED
SCIENCE NEWS**

www.advancedsciencenews.com

**ADVANCED
MATERIALS
INTERFACES**

www.advmatinterfaces.de

Figure 8. Influence of the addition of NaCl on the relative perimeter of a droplet comprising 20 mmol L^{-1} SA and 50 µmol L^{-1} CTAB and representation of the droplet after 900 s.

was chosen because it has been used successfully in a previous study to influence the particle morphology.[3a] **Table 2** specifies the viscosity of the PS-containing organic phase and **Figure 10** depicts the perimeter development for droplet injections corresponding to the same composition of the organic phase in an aqueous 50 µmol L^{-1} CTAB solution. The development of the fractal dimension is shown in Figure S8, Supporting Information. An increased shear viscosity results in a decreased deformation rate and perimeter. This shows that both the viscoelastic properties of the interface and the viscosity of the droplet bulk influence the interfacial deformation. Again, this behavior can be explained by the deformation properties of the interface, which are strongly influenced by

the viscosity of the oil phase.[2a,25] An increased viscosity counteracts the bending of the interface, which hinders the formation of long spines.

3.7. Injections with Other Surfactants and Nonpolar Phases

Interfacial instability was observed for various types of surfactants. **Table 3** presents an overview of several combinations of fatty acids and cationic quaternary ammonium surfactants and indicates whether droplet injections exhibit interfacial instability with the specialty of spine formation. All of the aqueous and non-aqueous solutions were below the saturation concentrations of the respective amphiphile and no crystallization was observed in the bulk solutions. Spine formation was only observed for cationic surfactants with carbon chains longer than 12 carbon atoms and fatty acids with carbon chains longer than 14 carbon atoms. For cationic surfactants with chain lengths longer than 12 carbon atoms, the growth rate increased with decreasing carbon chain length, which could potentially result from increased diffusion coefficients. The fastest growth rate and longest
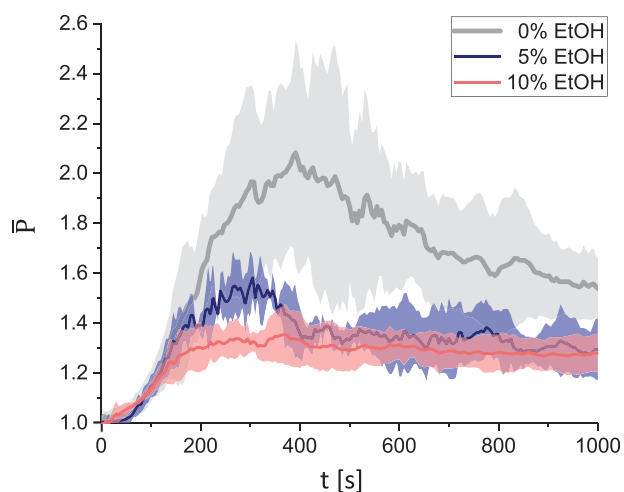

Figure 9. Influence of the addition of different amounts of ethanol on the relative perimeter of a droplet comprising 20 mmol L^{-1} SA in 50 µmol L^{-1} CTAB in ethanol/water mixtures.

Table 2. Shear viscosity of BCH solutions containing different amounts of PS at a shear rate of 100 s^{-1}.

PS concentration [%]	Viscosity [mPas]	s (Viscosity) [mPas]
0	2.63	0.03
10	13.66	0.03
20	32.38	0.02
30	242.80	0.92
40	851.97	2.03
50	4455.33	18.77

**ADVANCED
SCIENCE NEWS**

www.advancedsciencenews.com

**ADVANCED
MATERIALS
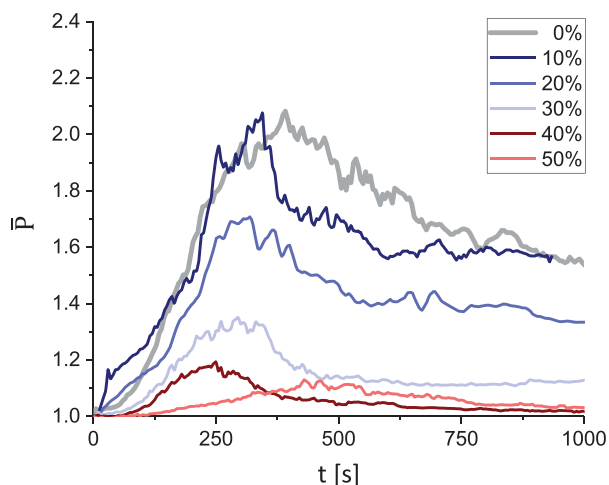INTERFACES**

www.advmatinterfaces.de

Figure 10. Influence of the PS concentration on the relative perimeter of a droplet comprising 20 mmol L^{-1} SA and 50 µmol L^{-1} CTAB. The standard deviation is shown in the corresponding diagram in Figure S8, Supporting Information.

spines were observed for SA. The choice of the fatty acid had a bigger effect on the maximum perimeter than the choice of the cationic surfactant.

The development of an interfacial instability with spine formation is tolerant to other nonpolar phases, as long as they exhibit low solubility in water. For a system comprising 20 mmol L^{-1} SA and 50 µmol L^{-1} CTAB, spine formation was observed for chlorobenzene, chlorocyclohexane, cyclohexane, benzene, tetrahydronaphthalene, and toluene, but not for chloroform, as it has a higher solubility in water.

4. Conclusion

In this study, we presented for the first time the analysis of a spine forming interfacial instability by digital image analysis of a 2D projection of an injection droplet. Using this procedure, it is possible to describe the droplet shape quantitatively using three parameters and to study the influence of various injection parameters on the temporal shape development. To the best of our knowledge, this approach is new in the study of liquid–liquid interfaces. We have demonstrated that the surfactant concentration, pH value, salt addition, ethanol concentration, and viscosity have a considerable impact on the morphology of this delicate and dynamic system. We hypothesize that the investigated parameters have an influence on the structure and composition of the condensed amphiphilic monolayer at the interface, thereby changing the viscoelastic properties of the interfacial membrane. The different properties of the membranes then manifest in various droplet shapes, which we have empirically investigated in the study.

To confirm this hypothesis, the study of the interfacial rheology would be necessary. The viscoelastic properties of liquid–liquid interfaces of mixed surfactants are usually measured using oscillating drop tensiometry.[26] However, owing to the prerequisite of a "non-dynamic" smooth interface, oscillating drop tensiometry is unsuitable for the proposed system. Approximating the presented system by creating SS/CTAB Langmuir monolayers at water/air interfaces and then measuring the viscoelastic properties could circumvent this problem.

Although the presented experiments are not designed to gain a complete understanding of the underlying mechanism, we suggest that the special morphologies are a result of an interplay between low interfacial tension and the elasticity

Table 3. Spine formation of several combinations of fatty acids and cationic quaternary ammonium surfactants.

Surfactant A[a]	Chain length A	Surfactant B[b]	Chain length B	Spine formation	$\bar{P}_{max}$	s($\bar{P}_{max}$)	$\bar{t}_{max,P}$	s($\bar{t}_{max,P}$)	$\bar{G}$	s($\bar{G}$)
Variation of cationic surfactant										
SA	18	STAB	18	Yes	1.98	0.31	503	129	12.63	6.90
SA	18	CTAB	16	Yes	2.22	0.39	394	127	19.93	6.97
SA	18	TTAB	14	Yes	2.14	0.72	214	30	32.74	23.46
SA	18	DTAB	12	No	–	–	–	–	–	–
Variation of fatty acid										
AA	20	CTAB	16	Yes	1.85	0.22	434	25	11.72	2.73
SA	18	CTAB	16	Yes	2.22	0.39	394	127	19.93	6.97
PA	16	CTAB	16	Yes	1.62	0.36	291	106	12.23	2.85
MA	14	CTAB	16	No	–	–	–	–	–	–
LA	12	CTAB	16	No	–	–	–	–	–	–
Other surfactants										
SA	18	DODAB	[18]$_2$	No	–	–	–	–	–	–
SA	18	DDDAB	[12]$_2$	No	–	–	–	–	–	–
SA	18	ECDAB	16	Yes	2.06	0.31	309	23	20.38	5.30
ODA	18	SDS	12	Yes	1.13	0.01	127	33	6.52	1.24

[a]Concentration of 20 mmol L^{-1} in BCH; [b]Concentration of 50 µmol L^{-1} in water.

of the droplet's interfacial monolayer as it has been observed elsewhere.[6]

In future studies precision measurements of the surface pressure using a Langmuir film balance would be suitable to quantitatively measure the influence of the subphase composition on the penetration dynamics of the CTAB molecules into the fatty acid monolayer.[12] Furthermore, Brewster angle microscopy could provide insights into the structure of the interfacial membranes.[25b,27]

The limitation of the proposed approach is that it relies heavily on the resolution of the imaging system. If the attributes are too small to be resolved by the microscope, they cannot contribute to the calculated perimeter increase, the FD, or the number of ejected droplets. Nevertheless, the present study provides new insights into the character of the spine forming interfacial instabilities and can potentially enable the precise tailoring of the surface morphology of solid particles that can be produced by such dynamic systems.

Supporting Information

Supporting Information is available from the Wiley Online Library or from the author.

Acknowledgements

Conflict of Interest

The authors declare no conflict of interest.

Data Availability Statement

The data that support the findings of this study are available from the corresponding author upon reasonable request.

Keywords

[1] a) B. A. Grzybowski, *Angew. Chem., Int. Ed.* **2011**, *50*, 40; b) A. Z. Patashinski, R. Orlik, K. Paclawski, M. A. Ratner, B. A. Grzybowski, *Soft Matter* **2012**, *8*, 1601; c) R. Granek, R. Ball, M. Cates, *J. Phys. II* **1993**, *3*, 829; d) W. D. Vedove, A. Sanfeld, *J. Colloid Interface Sci.* **1981**, *84*, 318; e) W. D. Vedove, A. Sanfeld, *J. Colloid Interface Sci.* **1981**, *84*, 328; f) W. D. Vedove, A. R. M. Garcia, A. Sanfeld, *J. Colloid Interface Sci.* **1983**, *95*, 299; g) O. Theissen, G. Gompper, *Eur. Phys. J. B* **1999**, *11*, 91.

[2] a) P. Erni, *Soft Matter* **2011**, *7*, 7586; b) Y. Sumino, N. L. Yamada, M. Nagao, T. Honda, H. Kitahata, Y. B. Melnichenko, H. Seto, *Langmuir* **2016**, *32*, 2891; c) Y. Sumino, H. Kitahata, H. Seto, K. Yoshikawa, *Phys. Rev. E* **2007**, *76*, 055202; d) Y. Sumino, H. Kitahata, H. Seto, K. Yoshikawa, *Soft Matter* **2011**, *7*, 3204.

[3] a) H. vom Stein, D. Volkmer, *Adv. Mater. Interfaces* **2021**, *8*, 2100628; b) D. Volkmer, S. Tugulu, M. Fricke, T. Nielsen, *Angew. Chem., Int. Ed.* **2003**, *42*, 58; c) J. Zhu, N. Ferrer, R. C. Hayward, *Soft Matter* **2009**, *5*, 2471; d) J. Zhu, R. C. Hayward, *J. Colloid Interface Sci.* **2012**, *365*, 275; e) N. Denkov, S. Tcholakova, I. Lesov, D. Cholakova, S. K. Smoukov, *Nature* **2015**, *528*, 392; f) S. Liu, R. Deng, L. Shen, X. Xie, J. Zhu, *Macromolecules* **2015**, *48*, 5944; g) S. Liu, R. Deng, W. Li, J. Zhu, *Adv. Funct. Mater.* **2012**, *22*, 1692; h) N. Wang, Y. Liao, R. Deng, S. Liu, N. Cao, B. Tan, J. Zhu, X. Xie, *Soft Matter* **2012**, *8*, 2697; i) Y. Wu, K. Wang, H. Tan, J. Xu, J. Zhu, *Langmuir* **2017**, *33*, 9889; j) K. H. Ku, J. M. Shin, H. Yun, G.-R. Yi, S. G. Jang, B. J. Kim, *Adv. Funct. Mater.* **2018**, *28*, 1802961; k) J. Zhu, R. C. Hayward, *Angew. Chem.* **2008**, *120*, 2143.

[4] a) C. Solans, D. Morales, M. Homs, *Curr. Opin. Colloid Interface Sci.* **2016**, *22*, 88; b) J. Santana-Solano, C. M. Quezada, S. Ozuna-Chacón, J. L. Arauz-Lara, *Colloids Surf., A* **2012**, *399*, 78; c) J. C. López-Montilla, P. E. Herrera-Morales, S. Pandey, D. O. Shah, *J. Dispersion Sci. Technol.* **2002**, *23*, 219.

[5] a) J. Gad, *Arch. Anat. Physiol.* **1878**, 181; b) J. W. McBain, T.-M. Woo, *Proc. R. Soc. A* **1937**, *163*, 182; c) W. Mansfield, *Aust. J. Chem.* **1952**, *5*, 331.

[6] S. Guttman, Z. Sapir, M. Schultz, A. V. Butenko, B. M. Ocko, M. Deutsch, E. Sloutskin, *Proc. Natl. Acad. Sci. U. S. A.* **2016**, *113*, 493.

[7] F. Caruso, *Adv. Mater.* **2001**, *13*, 11.

[8] a) Y. Wang, L. Shang, G. Chen, C. Shao, Y. Liu, P. Lu, F. Rong, Y. Zhao, *Appl. Mater. Today* **2018**, *13*, 303; b) N. Doshi, S. Mitragotri, *PLoS One* **2010**, *5*, e10051; c) K. Saralidze, L. H. Koole, M. L. W. Knetsch, *Materials* **2010**, *3*, 3537; d) G. Sharma, D. T. Valenta, Y. Altman, S. Harvey, H. Xie, S. Mitragotri, J. W. Smith, *J. Controlled Release* **2010**, *147*, 408; e) M. Cooley, A. Sarode, M. Hoore, D. A. Fedosov, S. Mitragotri, A. S. Gupta, *Nanoscale* **2018**, *10*, 15350; f) X. Zhu, C. Vo, M. Taylor, B. R. Smith, *Mater. Horiz.* **2019**, *6*, 1094; g) J. A. Champion, Y. K. Katare, S. Mitragotri, *J. Controlled Release* **2007**, *121*, 3.

[9] G. A. Silva, P. Ducheyne, R. L. Reis, *J. Tissue Eng. Regener. Med.* **2007**, *1*, 4.

[10] a) J.-H. Yang, Y.-S. Han, J.-H. Choy, *Thin Solid Films* **2006**, *495*, 266; b) F. Magalhães, R. M. Lago, *Sol. Energy* **2009**, *83*, 1521.

[11] M. T. Gokmen, F. E. Du Prez, *Prog. Polym. Sci.* **2012**, *37*, 365.

[12] V. B. Fainerman, D. Vollhardt, A. Roth, M. Fricke, D. Volkmer, *J. Phys. Chem. B* **2004**, *108*, 16163.

[13] D. R. Lide, *CRC Handbook of Chemistry and Physics*, 87th ed., CRC Press, Boca Raton, FL **2004**.

[14] W. S. Rasband, *ImageJ*, U. S. National Institutes of Health, Bethesda, Maryland, USA, **1997–2018**, https://imagej.nih.gov/ij/.

[15] A. Karperien, FracLac for ImageJ, https://imagej.nih.gov/ij/plugins/fraclac/FLHelp/Introduction.htm (accessed: November 2020).

[16] B. B. Mandelbrot, *Proc. Natl. Acad. Sci. USA* **1975**, *72*, 3825.

[17] R. Lopes, N. Betrouni, *Med. Image Anal.* **2009**, *13*, 634.

[18] a) D. Vollhardt, *Adv. Colloid Interface Sci.* **1996**, *64*, 143; b) A. Stocco, D. Carriere, M. Cottat, D. Langevin, *Langmuir* **2010**, *26*, 10663; c) A. Bonfillon, D. Langevin, *Langmuir* **1993**, *9*, 2172; d) L. R. Arriaga, D. Varade, D. Carriere, W. Drenckhan, D. Langevin, *Langmuir* **2013**, *29*, 3214.

[19] a) D. Langevin, *Adv. Colloid Interface Sci.* **2014**, *207*, 121; b) L. Lai, P. Mei, X.-M. Wu, L. Cheng, Z.-H. Ren, Y. Liu, *J. Surfactants Deterg.* **2017**, *20*, 565; c) C. Wang, X.-L. Cao, L.-L. Guo, Z.-C. Xu, L. Zhang, Q.-T. Gong, L. Zhang, S. Zhao, *Colloids Surf., A* **2016**, *509*, 601.

[20] A. W. Ralston, C. W. Hoerr, *J. Org. Chem.* **1942**, *07*, 546.

[21] D. Myers, *Surfaces, Interfaces, and Colloids: Principles and Applications*, 2nd ed., Wiley, New York **1999**.

[22] R. W. Smith, *Challenges in Mineral Processing*, Society of Mining Engineers, Littleton, CO **1989**.

[23] B. Kronberg, K. Holmberg, B. Lindman, *Surface Chemistry of Surfactants and Polymers*, John Wiley & Sons, UK **2014**.

[24] A. Li, S. H. Yalkowsky, *J. Pharm. Sci.* **1994**, *83*, 1735.

[25] a) D. Renggli, A. Alicke, R. H. Ewoldt, J. Vermant, *J. Rheol.* **2020**, *64*, 141; b) G. G. Fuller, J. Vermant, *Annu. Rev. Chem. Biomol. Eng.* **2012**, *3*, 519.

[26] R. Miller, J. K. Ferri, A. Javadi, J. Krägel, N. Mucic, R. Wüstneck, *Colloid Polym. Sci.* **2010**, *288*, 937.

[27] R. Johann, G. Brezesinski, D. Vollhardt, H. Möhwald, *J. Phys. Chem. B* **2001**, *105*, 2957.

2200264 (13 of 13)